Journal of Materials Chemistry A

Accepted Manuscript

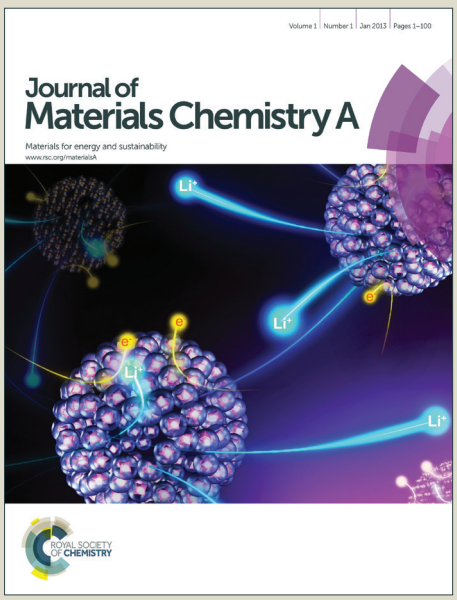

ROYAL SOCIETY OF CHEMISTRY

www.rsc.org/materialsA

Journal of Materials Chemistry A

Dynamic Article Links►

Cite this: DOI: 10.1039/c0xx00000x

ARTICLE TYPE

www.rsc.org/xxxxxx

Controllable synthesis of RGO/Fe_xO_y nanocomposites as a high-performance anode materials for lithium ion batteries

Xiangmao Dong,[a] Li Li,[b] Chongjun Zhao,*[a] Hua-Kun Liu[b] and Zaiping Guo*[b]

Received (in XXX, XXX) XthXXXXXXXXX 20XX, Accepted Xth XXXXXXXXX 20XX

DOI: 10.1039/b000000x

Graphene/metal oxide composites have attracted considerable attention for various applications, such as energy storage, catalysts, and electronics, however, the lack of effective and environmentally friendly fabrication methods for obtaining uniform graphene/metal oxide nanocomposites on a large scale has been one of the main technical barriers to real applications. We have developed a simple, efficient, and environmentally benign approach to the synthesis of reduced graphene oxide (RGO)/metal oxide composites via hydrothermal reaction of graphene oxide and metal powder under mild reaction conditions. For iron oxide as an example, by controlling the ratio of graphene oxide to Fe powder (m_{GO}/m_{Fe}), the hydrothermal temperature, and the addition of a mild oxidizing/reducing agent, the valence of Fe in the iron oxide products can be well tuned, i.e., various iron oxide/RGO composites, including RGO/Fe_3O_4, RGO/Fe_3O_4/Fe_2O_3, and RGO/Fe_2O_3, could be synthesized. RGO/Fe_xO_y composites in this study deliver a Li-ion storage capacity of 988.5 mA h g^{-1} at a current density of 100 mA g^{-1}. After cycling at 500 mA g^{-1} for 300 cycles, a capacity of 868.4 mA h g^{-1} can still be maintained (with no capacity decay). When the current density is 2000 mA g^{-1}, the capacity of 657.0 mA h g^{-1} is still retained, showing superior rate capability. The work described here provides a promising pathway to construct various graphene-based metal oxides as electrode materials for Li-ion batteries.

Introduction

The increasing demand for sustainable and renewable power sources in various applications such as hybrid vehicles, large memory backup devices, and renewable-energy power plants has stimulated intensive research efforts towards the development of various energy storage devices.[1-3] Lithium ion batteries (LIBs), with high energy density, high voltage, and environmental friendliness, have been seen as a most attractive power source to meet these concerns.[4-6] In order to satisfy the increasing demand for higher reversible capacities, metal oxides have been widely studied because they have higher theoretical capacity (~1000 mA h g^{-1}) than commercial graphite anodes (372 mA h^{-1}).[7] Their performance has been limited, however, due to the large volume expansion during cycling and poor electrical conductivity. Hence, various carbon additives have also been mixed with the metal oxide particles to solve the above problems. Among the various carbon materials pursued, two-dimensional graphene offers promising prospects and has attracted extensive attention, due to its high surface area, high flexibility, and electrical conductivity.[8] Moreover, reduced graphene oxide (RGO) can potentially be prepared on a large scale and at low cost. Among the main preparation methods for graphene, the chemical reduction of graphene oxide (GO) is considered a promising way to produce graphene in large volumes.[9] It is dangerous, however, and harmful to the environment to use hydrazine, dimethyl hydrazine, or other strong reductants to reduce graphene oxide to RGO.[10] In

addition, RGO prepared by hydrazine reduction may show a relatively low specific capacity.[11]

Recently, several kinds of active metal powder (Sn powder, Al powder, Zn powder, copper metal nanoparticles, and Fe powder) have been used as reducing agents, and the resultant RGO features high yield, low cost, and short processing time, apart from being eco-friendly.[10, 12, 10, 13-15] Among these, RGO/SnO_2, RGO/Cu_2O, and RGO/ZnO can be obtained by a direct redox reaction between graphene oxide (GO) and metal. Also, we have successfully prepared a series of transition metal oxide (TMO)/RGO composites by directly reacting metal powder with GO by a hydrothermal process (Mn_3O_4/RGO, Fe_2O_3/RGO, Co_3O_4/RGO, and ZnO/RGO).[16]

Among the metal oxides used for Li-ion batteries, iron oxides, such as Fe_2O_3 and Fe_3O_4, have received increased attention as very promising anode materials for rechargeable lithium-ion batteries (LIBs) because of their high theoretical capacity (1004 mA h g^{-1} for α-Fe_2O_3 and 924 mA h g^{-1} for Fe_3O_4), non-toxicity, low cost, and improved safety.[17] There are many reports on RGO/Fe_3O_4 or RGO/Fe_2O_3 for LIBs to take advantage of the outstanding properties of graphene that are mentioned above to improve volume variation and conductivity in Fe_xO_y. To the best of our knowledge, however, there are few reports on the lithium storage properties of their integrated electrodes. Bi-component metal oxides often integrate two types of functional materials that can demonstrate a strong synergistic effect, which enhances the intrinsic properties of each component, such as electric/ionic conductivity, electrochemical reactivity, and mechanical stability.[18] Recently, some groups reported that the bi-components often exhibits better battery properties than the single components, owing to the synergistic effect of the two types of functional materials.[19-21] With these considerations, we fabricated RGO/Fe_3O_4/Fe_2O_3 composites and used them as anode materials for lithium ion batteries.

Herein, we report an economically and environmentally friendly one-step method to synthesize RGO/Fe_xO_y composites through a hydrothermal route under mild conditions, which does not involve the use of any toxic reagents or acids. The influences of the mass ratio, m_{GO}/m_{Fe}, the temperature, and the mild oxidizing/reducing agent on the oxidation state of Fe, as well as the Li-storage properties of the as-obtained RGO/Fe_xO_y were systematically studied. Composites of RGO/Fe_3O_4, RGO/Fe_3O_4/Fe_2O_3, and RGO/Fe_2O_3 were prepared under well controlled conditions. As an anode material for Li-ion batteries, the specific capacity of RGO/Fe_3O_4/Fe_2O_3 is higher than those of RGO/Fe_2O_3 or RGO/Fe_3O_4 due to the above-mentioned advantages of bi-component metal oxides over their single-material counterparts.

Experimental section

Preparation of graphene – iron-oxide (GF) nanocomposites

All chemical reagents were analytical reagent (AR) grade and used as received. Graphene oxide (GO) was synthesized from natural graphite by a modified Hummers method.[22, 23] The composites were synthesized by varying the mass of graphene oxide (GO) as 30 mg, 60 mg, 90 mg, 120 mg, 150 mg, and 180 mg, and were denoted as GF30, GF60, GF90, GF120, GF150, and GF180, respectively. For GF120, the typical synthesis procedure is listed as follows: 120 mg GO was added to 50 ml of deionized (DI) water under ultrasonication, and 1 mmol (55.8 mg) Fe powder was then mixed with the aqueous solution of GO under ultrasonication. The resultant solution was transferred to a Teflon-lined stainless steel autoclave 100 mL in volume and was heated at 160 ºC for 24 h. Then, the composite was separated from the mixture by filtration, washed thoroughly with water and ethanol, and then collected and dried at 80 ºC for 12 h in vacuum. Pure RGO and Fe_xO_y were prepared through the same procedure, except without Fe powder or GO, respectively.

GF120-HP (with HP = hydrogen peroxide) or GF120-SB (with SB = sodium borohydride) were prepared under the same conditions as GF120, except that 2 ml H_2O_2 (30%) or 5 mmol $NaBH_4$ was added, respectively, after the Fe powder was mixed with the GO solution. The GF120-200 samples were prepared at 200 ºC instead of 160 ºC.

Characterization

Wide-angle (10°–80°) powder X-ray diffraction (XRD) was carried out using a polycrystalline X-ray diffractometer (RIGAKU, D/MAX 2550 VB/PC, 40 kV/200 mA, λ = 1.5406 Å). Thermogravimetric analysis was conducted on a TA 2000 Thermoanalyzer. Fourier transform infrared (FT-IR) spectra were collected on a NICOLET 6700 FTIR spectrophotometer. To demonstrate the particle size and morphology, all the samples were examined by field-emission scanning electron microscopy (FESEM, JEOL-7500, 2 keV) and transmission electron microscopy (TEM, JEOL-2010, 200 keV). Raman spectra were collected on an INVIA Raman microprobe (Renishaw

Instruments, England) with 514 nm laser excitation. X-ray photoelectron spectroscopy (XPS) measurements were performed on a Perkin-Elmer PHI5000CESCA system with a base pressure of 10^{-9} Torr.

Electrochemical measurements

The working electrodes were prepared by mixing the as-prepared samples, carbon black (Super P, MMM, Belgium), and poly (vinyl difluoride) (PVDF) in a weight ratio of 8:1:1 in an appropriate amount of N-methyl-2-pyrrolidone (NMP) as solvent to form a slurry. The resultant slurry was pasted on Cu foil and dried in a vacuum oven at 80 °C for 8 h. The electrodes were then pressed under approximately 200 kg cm^{-2} pressure and cut into disks before being assembled in an argon filled glove box with less than 1 ppm each of oxygen and moisture. The electrochemical measurements were carried out in CR2032 coin cells with Li foil as the counter electrode, 1 M $LiPF_6$ in ethylene carbonate (EC), dimethyl carbonate (DMC) and diethyl carbonate (DEC) (3:4:3 by volume) with 5 wt% fluoroethylene carbonate (FEC) additive as the electrolyte, and Celgard porous polypropylene membranes were used as separators. Cyclic voltammograms were collected on a VMP-3 electrochemical workstation at a scan rate of 0.1 mV s^{-1}. The discharge and charge measurements were conducted on a Land CT2001A battery tester.

Results and discussion

Characterization

Fig. 1 shows powder XRD patterns of the Fe_3O_4, GF30, GF120, and GF180 samples. For pure Fe_3O_4, there are seven diffraction peaks at 2θ = 30.0°, 35.4°, 43.0°, 53.4°, 56.9°, 62.5°, and 74.0°, which can be indexed with the (220), (311), (400), (422), (511), (440), and (533) planes (labelled as "•"), respectively. The peak positions of Fe_3O_4 and γ-Fe_2O_3 are similar, whereas the relative intensities of the peaks are different. The main peak of the Fe_3O_4 samples is located at 35.42°, consistent with the cubic phase of Fe_3O_4 (JCPDS no. 65-3107), while the main peak for γ-Fe_2O_3 is at 35.68°.[24] Meanwhile, two strong peaks at 2θ = 44.7° and 65.0°, which could be indexed to Fe (JCDS no. 06-0696), were also detected in the Fe_3O_4 pattern, indicating that the Fe powder was not completely converted to Fe_3O_4 after hydrothermal reaction for 24 h, but that Fe/Fe_3O_4 composite was formed. For comparison, the characteristic peaks of Fe_3O_4 in GF30 become more obvious in the composite samples, while the peaks of Fe become weaker, and a very weak peak at 2θ = 33.1° (ascribed to α-Fe_2O_3) can also be seen in the pattern, indicating that the Fe could be easily transformed into Fe_3O_4 in the presence of graphene oxide (GO). The GO diffraction peak (Fig. S1(a) in the Supporting Information) disappears, suggesting that the GO was reduced by the Fe powder. Meanwhile, Fe_3O_4 could be further oxidized to α-Fe_2O_3, as the mass of GO increased from 30 mg to 180 mg (Fig. 1(a) and Fig. S1(b)), while the ratio of Fe_3O_4 to Fe_2O_3 in the GF composites decreased in the GF60, 90, 120, and 150 RGO/Fe_3O_4/Fe_2O_3 composites, which could be confirmed by the Raman and IR spectra discussed below. To calculate the amount of Fe_2O_3 and Fe_3O_4 quantitatively, the weight fraction of Fe_2O_3 in the GF120 composite was determined to be ~0.776 according the intensities of the groups of peaks in the XRD data. [25-27] For the GF180 composite, the characteristic peaks around 2θ = 24.1°, 33.0°, 35.6°, 40.8°, 43.2°, 49.5°, 54.0°, 57.6°, 62.3°, 64.0°, 71.8°, and 75.5° can be indexed to the (012), (014), (110), (113), (202), (024), (116), (018), (214), (300), (101), and (220) lattice planes (labelled as "*") of typical peaks of α-Fe_2O_3 (JCPDS no. 33-0664), respectively. No other peaks remained for GF180, suggesting that the GF180 composite is pure RGO/Fe_2O_3.

The influence of temperature and the mild oxidizing/reducing agent on the final Fe oxidation state was also investigated. When the hydrothermal temperature was fixed at 200 ºC instead of 160 ºC, the GF120 samples were also pure RGO/Fe_2O_3 (Fig. S1(c)), indicating that Fe tends to be oxidized to a higher oxidation state (Fe_2O_3) at a higher temperature. After adding hydrogen peroxide or sodium borohydride, pure Fe_2O_3/RGO and Fe_3O_4/RGO could also be prepared successfully (Fig. S1(c)), and this could be the reason why the oxidation state of Fe is affected by GO and by the O_2 in the top empty space and in the solution.[16] For all the GF samples, a diffraction hump appears between 20° and 30° in the powder XRD pattern of the composite, which may have originated from the graphene nanosheets and becomes more obvious as the mass of GO increases (Fig. 1 and Fig. S1(b)). As shown in Fig. S1(d), the RGO contents were determined by TGA to be about 21.61wt%, 44.20wt%, and 50.34wt% for GF30, GF120, and GF180, respectively.

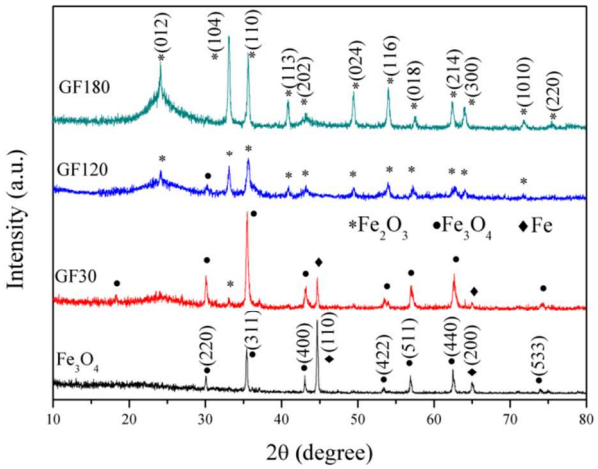

Fig. 1 XRD patterns of GF30, GF120, GF180, and pure Fe_3O_4.

The Raman spectra of Fe_3O_4, GF30, GF120, and GF180 are presented in Fig. 2, which clearly shows that there are two broad peaks in the GF samples. The peak at 1590 cm^{-1} (G band) is related to the vibration of sp^2-bonded carbon atoms, and the peak at 1350 cm^{-1} (D band) is related to the defects. It is obvious that the intensity ratios of the D to the G band (I_D/I_G) for the GF samples (GF30: 1.44; GF120: 1.18; GF180: 1.10) are much higher than for GO and RGO (GO: 0.89; RGO: 0.95) (Fig. S2), which can further confirm the reduction of GO[28] suggested in the XRD results. For the pure Fe_3O_4 sample, a strong signal at 670 cm^{-1}, accompanied by other weak features around 293 and 543 cm^{-1}, can be easily observed, and these three peaks can be assigned to the E_g, T_{2g}, and A_{1g} vibrational modes, respectively.[29] With increasing ratio of m_{GO}/m_{Fe}, the main peak of Fe_3O_4 becomes weaker, e.g., for the GF180 composite, there are no peaks remaining around 670 cm^{-1}, instead, the fundamental Raman bands at 223, 242, 288, 405, 498, and 606 cm^{-1} are observed, which can be assigned to the $2A_{1g}$ and $4E_g$ Raman modes for the typical hematite phase of pure α-Fe_2O_3 particles.[30] For GF120, there is an additional weak peak at 665 cm^{-1} compared to GF180 (inset of Fig. 2), indicating that GF120 contains both Fe_3O_4 and α-Fe_2O_3, which is consistent with the XRD results and previous reports.[31, 32]

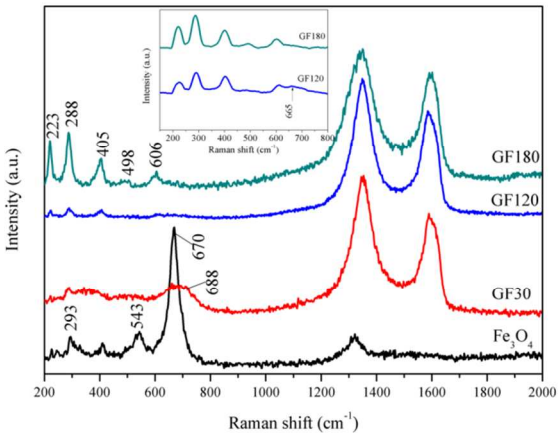

Fig. 2 Raman spectra of GF30, GF120, GF180, and Fe_3O_4. Inset: enlargement of Raman spectra of GF120 and GF180 for the indicated range.

Fig. 3 shows the FT-IR spectra of the GF30, GF120, and GF180 composites and of the Fe_3O_4. All the GF samples show absorption peaks at 3432, 1564, 1401, and 1021 cm^{-1}, corresponding to the vibrations of the O-H, C=C, C-H, and C-O functional groups on the graphene nanosheet (GNS) surface.[33] Compared with RGO (Fig. S3), pure Fe_3O_4 and GF30 have two new peaks at 571 and 466 cm^{-1}, marked by the dotted lines, which are attributable to the stretching vibrations of Fe–O in the crystalline lattice of Fe_3O_4.[34] For GF180, the two peaks located at 542 and 461 cm^{-1} likewise represent the stretching vibrations of Fe–O in α-Fe_2O_3.[35] There are four peaks for GF120 (Fig. 3), however, which can be explained by assuming that there are two binding modes between Fe and O, which can also be seen in the spectra of GF60, GF90, and GF150 (Fig. S3). These indicate that GF60, GF90, GF120, and GF150 are RGO/Fe_3O_4/Fe_2O_3 composites, which is consistent with the XRD and Raman results.

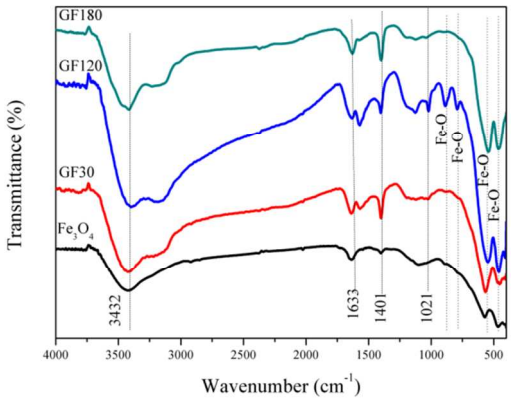

Fig. 3 FT-IR spectra of GF30, GF120, GF180, and Fe_3O_4.

XPS (Fig. 4(a)) analysis shows the presence of Fe, O, and C in the GF180 composite, and the C 1s spectrum of GO in Fig.

4(b) contains three components: non-oxygenated C-C (284.8 eV), C-O species (286.9 eV), and C=O species (288.8 eV). The components associated with oxygenated groups markedly decrease for GF180 (in Fig. 4(c)), which is a clear indication of the reduction of GO. In Fig. 4(d), the peaks of the Fe_3O_4 sample for Fe $2p_{3/2}$ and Fe $2p_{1/2}$ appear at 711.4 and 724.9 eV. It has been reported that the Fe $2p_{3/2}$ spectrum for Fe_3O_4 does not have satellite peaks,[36] demonstrating the presence of Fe_3O_4 in the GF30 composite. In addition to the Fe $2p_{3/2}$ and Fe $2p_{1/2}$ peaks, there is also a satellite peak for GF180 and GF120 at 719.4 eV, which is characteristic of Fe_2O_3,[37] suggests that Fe_2O_3 exists in GF180 and GF120. The XPS spectra are well corroborated by the previous results and reveal that the GF composites have been synthesized successfully.

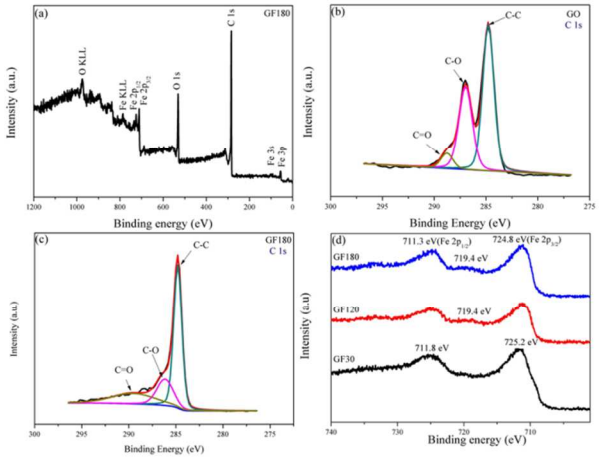

Fig. 4 XPS spectra: (a) survey scan of GF180, C 1s spectra of (b) GO and (c) GF180, and (d) Fe 2p peaks of GF180, GF120, and GF30.

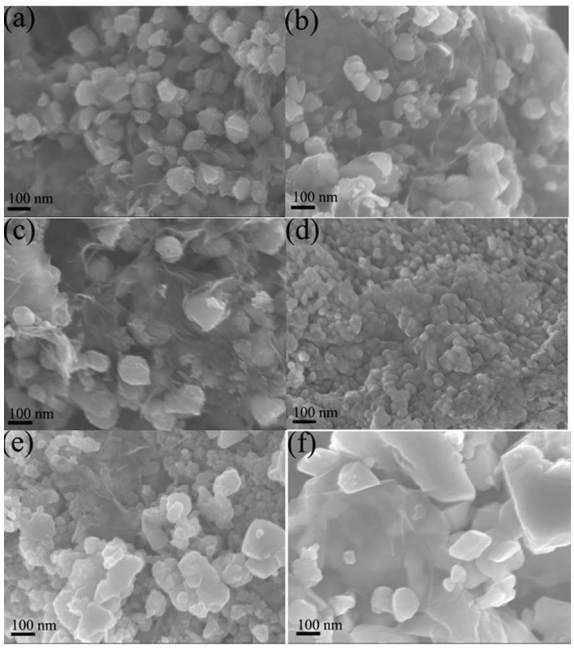

Fig. 5 FESEM images of (a) GF30, (b) GF120, (c) GF180, (d) GF120-HP, (e) GF120-SB, and (f) GF120 synthesized at 200 ºC (GF120-200).

Fig. 5 presents FESEM images of the RGO/Fe_xO_y composites prepared under different conditions. In the images, both iron oxide nanoparticles and wrinkled sheet-like structures of RGO can be clearly observed. Moreover, the metal oxide nanoparticles are well dispersed and mixed with the sheet-like RGO, which inhibits aggregation of the iron oxide particles and enlarges the contact area between the iron oxides and the electrolyte. In Fig. 5(a-c), it is evident that two-dimensional GNS are well decorated by a large number of spherical Fe_3O_4 or Fe_2O_3 nanostructures. The morphology of RGO/Fe_xO_y distinctly changes when the synthesis conditions change. As shown in Fig. 5(d), when the H_2O_2 was added, the Fe_2O_3 particles became small and uniform, while the size of the iron oxide particles obviously increased when SB was used as the reductant or a high temperature of 200 ºC was used, as shown for GF120-SB and GF200 in Fig. 5(e) and (f).

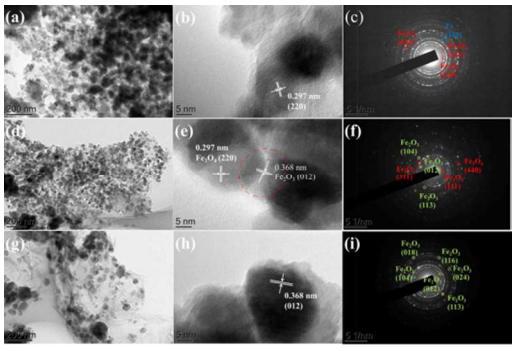

Fig. 6 TEM images (left), HRTEM images (middle), and SAED patterns (right), respectively, of (a)-(c) GF30 nanocomposite, (d)-(f) GF120 nanocomposite, and (g)-(i) GF180 nanocomposite.

As shown in the TEM images (Fig. 6(a, d, g)) of different RGO/Fe_xO_y composites, the two-dimensional (2D) graphene sheets are well decorated by a large quantity of iron oxide nanoparticles, and the outlines of both the graphene and the iron oxide nanoparticles can be clearly observed. The homogeneously distributed graphene sheets among the iron oxide nanoparticles not only act as a good conductive network throughout the composite, but also protect the iron oxide nanoparticles from agglomeration, which plays a key role in facilitating better cycling performance than in conventional iron oxide based devices. The high resolution TEM (HRTEM) image in Fig. 5(b) shows the interfacial structure between the Fe_3O_4 nanoparticles and graphene. The crystal lattice fringes with a *d*-spacing of 0.297 nm come from the (220) planes of Fe_3O_4. We also confirmed the clear formation of Fe_3O_4 and residual Fe in the selected area electron diffraction (SAED) pattern shown in Fig. 6(c). For sample GF120, the *d*-spacing of 0.368 nm comes from the (012) planes of Fe_2O_3 (indicated by dashed red circle) and can be seen in addition to that characteristic of Fe_3O_4 (Fig. 6(e)). The SAED pattern of GF120 further confirms this result, as the phase of the GF composite was transformed to a mixture of Fe_2O_3 and Fe_3O_4 when GO was increased to a quantity of 120 mg. Only Fe_2O_3 exists in the GF180 composite (Fig. 6(h, i)).

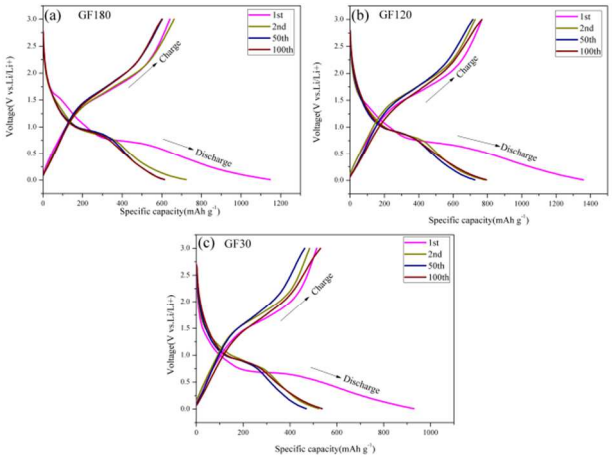

Fig. 7 Galvanostatic charge/discharge profiles for selected cycles of (a) GF180, (b) GF120, and (c) GF120 nanocomposites at the current density of 500 mA g^{-1} within the potential window from 0.1 V to 3 V.

We also demonstrated the effectiveness of these GF materials for improving the lithium storage performance. The electrochemical performance of the GF180, GF120, and GF30 composites was evaluated by galvanostatic discharge–charge measurements at a current density of 500 mA g^{-1} in the voltage range of 0.01–3 V vs. Li^+/Li (Fig. 7(a-c)). At the first cycle, all the discharge curves of RGO/Fe_2O_3 (GF180), RGO/Fe_3O_4/Fe_2O_3 (GF120), and RGO/Fe_3O_4 (GF30) show similar plateaus at ~ 0.75 V, corresponding the reduction of Fe^{3+} and/or Fe^{2+} to Fe^0.[38] There are no obvious differences among the discharge curves of these three composites, since Fe_2O_3 and Fe_3O_4 undergo a similar kind of metallic reduction i.e. conversion reaction,[39] and the reaction mechanism of Fe_xO_y could be proposed as follows:

$$\alpha\text{-}Fe_2O_3 + 6Li^+ + 4e^- \leftrightarrow 2Fe^0 + 3Li_2O \quad (1)$$

$$Fe_3O_4 + 8Li^+ + 8e^- \leftrightarrow 3Fe^0 + 4Li_2O \quad (2)$$

Although the content of Fe_xO_y in GF120 is not the highest (Fig. S1(d)), the plateau of RGO/Fe_2O_3/Fe_3O_4 (GF120) at 0.8 V is the longest among three samples, which may be due to a strong synergistic effect between the Fe_2O_3 and Fe_3O_4 components in the right composition. As shown in Fig. 7(b), the initial charge and discharge capacities of the GF120 electrode are 767.4 and 1359.0 mA h g^{-1}, respectively, corresponding to a coulombic efficiency of 56.5%. The capacity loss of ~43.5% for GF120 electrode may be due to the irreversible reactions between lithium ions and the functional groups on the graphene sheets, as well as the decomposition of the electrolyte solvent to form the solid electrolyte interphase (SEI) layer, all of which are common for most anode materials, especially nanostructured ones.[40, 41] From the second cycle onwards, the GF120 electrode exhibits a high discharge capacity of 783.5 mA h g^{-1}, which then stabilizes at about 868.4 mA h g^{-1} after 300 cycles with a high coulombic efficiency of nearly 100% (Fig. 8(a)), while GF180 and GF30 exhibited lower reversible specific capacities.

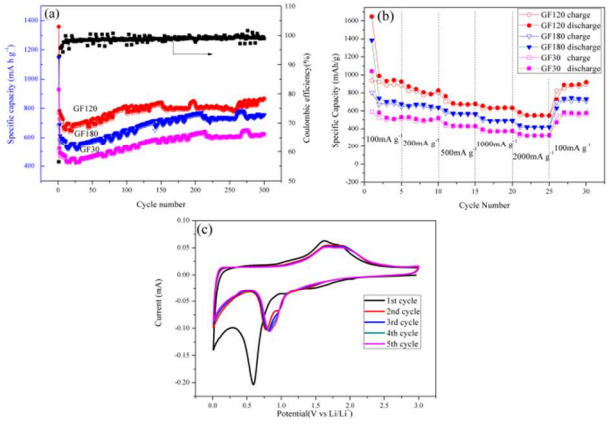

Fig. 8 (a) Comparison of the cycling performance for GF180, GF120, and GF30. (b) Rate capacity of GF180, GF120, and GF30. (c) Cyclic voltammograms of RGO/Fe_3O_4/Fe_2O_3 (GF120) composite for the 1st, 2nd, 3rd, 4th, and 5th cycles at a scan rate of 0.1 mV s^{-1}.

It can be seen from Fig. 8(a) that the cycling performance of the GF120 electrode is excellent, as there is no capacity loss after 300 cycles at a current density of 500 mA g^{-1}. The increasing trend in the capacity of the GF120 composite electrode may be attributed to either the reduced nanoparticle size (by an electrochemical milling effect), which could expose more electrochemically active sites to the electrolyte[42] or the reversible growth of a polymeric gel-like film resulting from kinetically activated electrolyte degradation[43] and the improvement of lithium ion accessibility and accommodation behaviour in the hybrid during the cycling process.[43, 44] Obviously, GF120 exhibited the highest reversible specific capacity among the three GF composites. The possible reasons are as follows:

When the mass of GO increases from 30 mg to 120 mg, the increasing amount of RGO can prevent the agglomeration of iron oxide particles, and this causes a uniform distribution of Fe_xO_y in the GF composites. The RGO networks that exist in the composites play an important role in electrochemical performance, since they can promote electronic transport and maintaining the structural integrity,[44] leading to a higher specific capacity for GF120 compared to GF30. As the mass of GO increases from 120 to 180 mg, however, the restacking of RGO sheets could occur, which leads to less utilization of the electrochemical activity of graphene[45] (Figs. 5 and 6), while the lithium consumption by the formation of SEI increases with increasing RGO content;[44] Also, with increasing GO content, more of the iron oxide in the composite is α-Fe_2O_3, which has relatively low electrical conductivity compared to Fe_3O_4,[46] with both of the above reasons leading to the lower specific capacity of GF180 compared to GF120.

In addition, the GF120 composite shows good rate performance as well (Fig. 8(b)), which is beneficial for its successful practical application as anode electrode. A discharge capacity of 988.5 mA h g^{-1} at the current density of 100 mA g^{-1}, 872.0 mA h g^{-1} at 200 mA g^{-1}, 763.4 mA h g^{-1} at 500 mA g^{-1}, and 657.0 mA h g^{-1} at 1000 mA g^{-1} are obtained, respectively. Even with cycling at 2000 mA g^{-1}, GF120 can still retain a charge capacity of 585.8 mA h g^{-1}, which can be further restored to 919.8 mA h g^{-1} at a current density of 100 mA g^{-1} in five cycles, displaying good rate performance. All of these values are higher than the capacity of the GF180 or GF30 electrode at the same current densities.

To discover the electrochemical reaction involved in lithium storage in RGO/Fe_3O_4/Fe_2O_3 composite, cyclic voltammetry (CV) was conducted on the cell with GF120 at room temperature in the 0.01–3.0 V range and a scan rate of 0.1 mV s^{-1}, as shown in Fig. 8(c). In the 1st cycle, the cathodic peaks at 0.65 V and 1.1 V corresponds to the reduction of Fe^{3+} or Fe^{2+} to Fe^0 and the irreversible reaction with the electrode.[47] The peak that is observed at 1.38 V may be ascribed to the formation of $Li_xFe_3O_4$, and it disappears in the subsequent cycles. In the anodic scan, two broad peaks were recorded at 1.64 V and 1.85 V, which are assignable to the oxidation of Fe^0 to Fe^{2+} and Fe^{3+}, respectively.[48] In the subsequent cycles, the obvious cathodic peak at 0.65 V was shift to 0.8 V due to the polarization, while the oxidation peak shows no change, indicating improved reaction kinetics. Importantly, after the first cycle, both the CV peak positions and the integrated areas remain almost unchanged, indicating relatively good capacity retention.[49]

The reasons for the outstanding electrochemical performance of GF120 can be explained as follows: 1) The RGO sheets provide a highly electrically conductive matrix for the composite, which reduces the internal resistance of the LIBs and is favourable for stabilizing the electronic and ionic conductivity, thereby leading to high specific capacity and cyclability.[45] 2) RGO nanosheets can shorten the path length for Li-ion transport,[45] increase the active material/electrolyte contact area, and facilitate the Li-ion diffusion to sites on the surface of the Fe_xO_y nanostructures. Meanwhile, the presence of Fe_xO_y nanostructures on the graphene nanosheets effectively prevents the agglomeration of graphene nanosheets, and thus maintains their high active surface area, which is favourable for increasing the Li storage capacity of the graphene nanosheets in the nanocomposites. 3) The well mixed composite structure maintains good electrical conductivity in the composites,[50] which provides an elastic buffer space to accommodate the volume expansion/contraction (avoiding cracking or crumbling) of the Fe_xO_y nanostructures during Li insertion/extraction processes, but also efficiently prevents the aggregation of the Fe_xO_y nanostructures during continuous cycling, thereby maintaining good battery performance.[51] 4) The presence of a small fraction of Fe_3O_4 in the nanostructured electrode, due to its higher

electrical conductivity compared to that of α-Fe_2O_3, could enhance the overall electrical conductivity on the local domain and is beneficial to the electronic conductivity of the entire electrode.

Conclusions

RGO/Fe_3O_4, RGO/Fe_3O_4/Fe_2O_3, and RGO/Fe_2O_3 were successfully fabricated by controlling the ratio of graphene oxide to metal, the temperature, or the type of mild reactant. The valence of Fe in the iron oxide products can be well tuned under mild reaction conditions. The GF120 composite exhibits a maximal capacity of 988.5 mA h g^{-1} at a current density of 100 mA g^{-1}. It shows good capacity retention, with 868.4 mA h g^{-1} after the 300th discharge at a current density of 500 mA g^{-1}, as well as 585.8 mA h g^{-1} of discharge capacity even at the current density of 2000 mA g^{-1}. The total specific capacity of GF120 is higher than those of GF180 or GF30, indicating the positive synergistic effect of Fe_2O_3 and Fe_3O_4 towards the improvement of electrochemical performance. This method provides a new direction towards the fabrication of other RGO/metal oxides for various applications.

Acknowledgements

Financial support was provided by the National Natural Science Foundation of China (No.20504026), the Shanghai Natural Science Foundation (No. 13ZR1411900), the Shanghai Leading Academic Discipline Project (B502), and the Shanghai Key Laboratory Project (08DZ2230500). The authors would like to thank Dr Tania Silver for critical reading of the manuscript.

Notes and references

[a]*Key Laboratory for Ultrafine Materials of Ministry of Education, Shanghai Key Laboratory of Advanced Polymeric Materials, School of Materials Science and Engineering, East China University of Science and Technology, Shanghai 200237, PR China. Fax: 86 21 6425 0838; Tel: 86 21 6425 0838; E-mail: chongjunzhao@ecust.edu.cn*

[b]*Institute for Superconducting and Electronic Materials, University of Wollongong, Wollongong, NSW 2522 Australia. Fax: 61 2 42215731; Tel: 61 2 42215225; E-mail: zguo@uow.edu.au*

*†Electronic Supplementary Information (ESI) available: See DOI: **10.1039/b000000x/***

1. J. R. Miller and P. Simon, *Science*, 2008, **321**, 651-652.
2. P. Simon and Y. Gogotsi, *Nat. mater.*, 2008, **7**, 845-854.
3. C. Liu, F. Li, L. P. Ma and H. M. Cheng, *Adv. Mater.*, 2010, **22**, E28-E62.
4. J.-M. Tarascon and M. Armand, *Nature*, 2001, **414**, 359-367.
5. K. Kang, Y. S. Meng, J. Bréger, C. P. Grey and G. Ceder, *Science*, 2006, **311**, 977-980.
6. M. Armand and J.-M. Tarascon, *Nature*, 2008, **451**, 652-657.
7. H. B. Wu, J. S. Chen, H. H. Hng and X. W. D. Lou, *Nanoscale*, 2012, **4**, 2526-2542.
8. G. Zhao, L. Jiang, Y. He, J. Li, H. Dong, X. Wang and W. Hu, *Adv. Mater.*, 2011, **23**, 3959-3963.
9. Y. Zhu, S. Murali, M. D. Stoller, K. J. Ganesh, W. Cai, P. J. Ferreira, A. Pirkle, R. M. Wallace, K. A. Cychosz, M. Thommes, D. Su, E. A. Stach and R. S. Ruoff, *Science*, 2011, **332**, 1537-1541.
10. Z. Fan, K. Wang, T. Wei, J. Yan, L. Song and B. Shao, *Carbon*, 2010, **48**, 1686-1689.
11. Y. Wang, Z. Shi, Y. Huang, Y. Ma, C. Wang, M. Chen and Y. Chen, *J. Phys. Chem. C*, 2009, **113**, 13103-13107.
12. M. Chen, C. Zhang, L. Li, Y. Liu, X. Li, X. Xu, F. Xia, W. Wang and J. Gao, *ACS Appl. Mater. Interfaces*, 2013, 5, 13333-13339.
13. X. Mei and J. Ouyang, *Carbon*, 2011, **49**, 5389-5397.
14. W. Tao, G. Jianping, X. Xiaoyang, W. Wei, G. Chunjuan and Q. Haixia, *Nanotechnology*, 2013, **24**, 215604.
15. Z.-J. Fan, W. Kai, J. Yan, T. Wei, L.-J. Zhi, J. Feng, Y.-m. Ren, L.-P. Song and F. Wei, *ACS Nano*, 2010, **5**, 191-198.
16. C. Zhao, S.-L. Chou, Y. Wang, C. Zhou, H.-K. Liu and S.-X. Dou, *RSC Adv.*, 2013, **3**, 16597-16603.
17. L. Zhang, H. B. Wu and X. W. D. Lou, *Adv. Energy Mater.*, 2013.
18. J. Jiang, Y. Li, J. Liu, X. Huang, C. Yuan and X. W. D. Lou, *Adv. Mater.*, 2012, **24**, 5166-5180.
19. L. Hu, Y. Huang, F. Zhang and Q. Chen, *Nanoscale*, 2013, **5**, 4186-4190.
20. W. Zhou, C. Cheng, J. Liu, Y. Y. Tay, J. Jiang, X. Jia, J. Zhang, H. Gong, H. H. Hng and T. Yu, *Adv. Funct. Mater.*, 2011, **21**, 2439-2445.
21. Y. Wang, J. Xu, H. Wu, M. Xu, Z. Peng and G. Zheng, *J. Mater. Chem.*, 2012, **22**, 21923-21927.
22. W. S. Hummers and R. E. Offeman, *J. Am. Chem. Soc.*, 1958, **80**, 1339-1339.
23. Y. Xu, H. Bai, G. Lu, C. Li and G. Shi, *J. Am. Chem. Soc.*, 2008, **130**, 5856-5857.
24. Q. Peng, J. Gan, S. Wang, L. Kong, G. Chen, Y. Yang and G. Huang, *Ind. Eng. Chem. Res.*, 2013, **52**, 7713-7717.
25. V. Esteve, L. E. Ochando, M. M. Reventós, G. Peris and J. M. Amigó, *Cryst. Res. Technol.*, 2000, **35**, 1183-1192.
26. V. J. Hurst, P. A. Schroeder and R. W. Styron, *Anal. Chim. Acta*, 1997, **337**, 233-252.
27. A. L. Ortiz, F. Sánchez-Bajo, N. P. Padture, F. L. Cumbrera and F. Guiberteau, *J. Eur. Ceram. Soc.*, 2001, **21**, 1237-1248.
28. J. Zhu, T. Zhu, X. Zhou, Y. Zhang, X. W. Lou, X. Chen, H. Zhang, H. H. Hng and Q. Yan, *Nanoscale*, 2011, **3**, 1084-1089.
29. T. Muraliganth, A. Vadivel Murugan and A. Manthiram, *Chem. Commun.*, 2009, 7360-7362.
30. D. L. A. de Faria, S. Venâncio Silva and M. T. de Oliveira, *J. Raman Spectrosc.*, 1997, **28**, 873-878.
31. S. Motozuka, M. Tagaya, H. Nishiyama, M. Nishikawa, T. Ikoma, T. Yoshioka, S. Samitsu and J. Tanaka, *J. Phys. Chem. C*, 2013, **117**, 9908-9919.
32. J. E. Maslar, W. S. Hurst, W. J. Bowers, J. H. Hendricks and M. I. Aquino, *J. Electrochem. Soc.*, 2000, **147**, 2532-2542.

33. H. Li, G. Zhu, Z.-H. Liu, Z. Yang and Z. Wang, *Carbon*, 2010, **48**, 4391-4396.
34. B. Li, H. Cao, J. Shao, M. Qu and J. H. Warner, *J. Mater. Chem.*, 2011, **21**, 5069-5075.
35. D. Wang, Y. Li, Q. Wang and T. Wang, *J. Solid State Electrochem.*, 2012, **16**, 2095-2102.
36. D. D. Hawn and B. M. DeKoven, *Surf. Interface Anal.*, 1987, **10**, 63-74.
37. X. Zhu, Y. Zhu, S. Murali, M. D. Stoller and R. S. Ruoff, *ACS Nano*, 2011, **5**, 3333-3338.
38. P. Poizot, S. Laruelle, S. Grugeon, L. Dupont and J. Tarascon, *Nature*, 2000, **407**, 496-499.
39. M. Biswal, A. Suryawanshi, V. Thakare, S. Jouen, B. Hannoyer, V. Aravindan, S. Madhavi and S. Ogale, *J. Mater. Chem. A*, 2013, **1**, 13932-13940.
40. W. M. Zhang, X. L. Wu, J. S. Hu, Y. G. Guo and L. J. Wan, *Adv. Funct. Mater.*, 2008, **18**, 3941-3946.
41. W. Wei, S. Yang, H. Zhou, I. Lieberwirth, X. Feng and K. Müllen, *Adv. Mater.*, 2013, **25**, 2909-2914.
42. Y. Yang, X. Fan, G. Casillas, Z. Peng, G. Ruan, G. Wang, M. J. Yacaman and J. M. Tour, *ACS Nano*, 2014.
43. G. Zhou, D.-W. Wang, F. Li, L. Zhang, N. Li, Z.-S. Wu, L. Wen, G. Q. Lu and H.-M. Cheng, *Chem. Mater.*, 2010, **22**, 5306-5313.
44. Y. Chang, J. Li, B. Wang, H. Luo, H. He, Q. Song and L. Zhi, *J. Mater. Chem. A*, 2013, **1**, 14658-14665.
45. Z.-S. Wu, G. Zhou, L.-C. Yin, W. Ren, F. Li and H.-M. Cheng, *Nano Energy*, 2012, **1**, 107-131.
46. K. K. Lee, S. Deng, H. M. Fan, S. Mhaisalkar, H. R. Tan, E. S. Tok, K. P. Loh, W. S. Chin and C. H. Sow, *Nanoscale*, 2012, **4**, 2958-2961.
47. J. Z. Wang, C. Zhong, D. Wexler, N. H. Idris, Z. X. Wang, L. Q. Chen and H. K. Liu, *Chem. - Eur. J.*, 2011, **17**, 661-667.
48. L. Li, G. Zhou, Z. Weng, X.-Y. Shan, F. Li and H.-M. Cheng, *Carbon*, 2014, **67**, 500-507.
49. G. Zhou, D.-W. Wang, P.-X. Hou, W. Li, N. Li, C. Liu, F. Li and H.-M. Cheng, *J. Mater. Chem.*, 2012, **22**, 17942-17946.
50. W. Lv, F. Sun, D.-M. Tang, H.-T. Fang, C. Liu, Q.-H. Yang and H.-M. Cheng, *J. Mater. Chem.*, 2011, **21**, 9014-9019.
51. S.-M. Paek, E. Yoo and I. Honma, *Nano Lett.*, 2008, **9**, 72-75.